

Supplementary Information to the publication in *Chemical Communication* **2022**:

Aliovalent Anion Substitution as a Design Concept for Heteroanionic Ruddlesden-Popper Hydrides

Nicolas Zapp,^a Florian Oehler,^b Marko Bertmer,^c Henry Auer,^d Denis Sheptyakov,^e Clemens Ritter^f and Holger Kohlmann^{*a} * Correspondence author: holger.kohlmann@uni-leipzig.de

[a] Institute of Inorganic Chemistry, Leipzig University, Johannisallee 29, 04103 Leipzig, Germany.

[b] Institute of Inorganic Chemistry, Halle-Wittenberg University, Kurt-Mothes-Str. 2, 06120 Halle (Saale), Germany.

[c] Felix-Bloch-Institute for Solid-State Physics, Leipzig University, Linnéstr. 5, 04103 Leipzig, Germany.

[d] Department of Mobile Energy Storage and Electrochemistry, Fraunhofer Institute for Ceramic Technologies and Systems IKTS, Winterbergstraße 28, 01277 Dresden

[e] Laboratory for Neutron Scattering and Imaging, Paul Scherrer Institut, 5232 Villigen, Switzerland

[f] Institut Laue-Langevin, 71 avenue des Martyrs, CS 20156, 38042 Grenoble Cedex 9, France

Table of Contents

Table of Contents	S1
Experimental Procedures.....	S2
Synthesis	S2
Elemental Analysis	S3
X-ray Powder Diffraction (XRPD).....	S3
Neutron Powder Diffraction (NPD).....	S4
Rietveld Analysis	S4
Density Functional Theory (DFT) Calculations.....	S5
Impedance Spectroscopy.....	S5
Nuclear Magnetic Resonance (NMR) Spectroscopy.....	S6
Results and Discussion.....	S7
LiLa ₂ NH ₂ O and LiLa ₂ ND ₂ O	S7
Synthesis and XRPD Analysis	S7
Crystal Structure Analysis	S10
LiLa ₂ N _{1.5} H _{2.5} and LiLa ₂ N _{1.5} D _{2.5}	S11
Synthesis and XRPD Analysis	S11
Crystal Structure Analysis	S12
Crystal Structure Discussion	S13
LiLa ₂ DO ₃ and LiSrLaD ₂ O ₂	S14
Density of States (DOS)	S16
Impedance Spectroscopy	S18
NMR Spectroscopy.....	S21
References	S25
Author Contributions.....	S27

Experimental Procedures

Synthesis

All samples were handled in an argon (Alphagaz, 99.999% purity) filled glovebox whose O₂ and H₂O levels were kept below 1 ppm. All powders were ground thoroughly in agate mortars prior and after synthesis and characterized by X-ray powder diffraction, whereas the nitrides required initial crushing in a stainless steel or tungsten carbide mortar after synthesis. Stainless steel tubes were sealed by pressing in the glovebox and subsequent arc welding in 40 kPa argon atmospheres. They were then placed in a dynamically evacuated silica glass tube ($p < 10$ Pa) for annealing.

LaH₃ and LaD₃ were obtained from surface-cleaned lanthanum ingots (Smart Elements, 99.9% trace rare earth metals basis) which were annealed at 650 K for 2 h and subsequently at 520 K for 48 h under H₂ (Air Liquide, 99.9%) or D₂ (Air Liquide, 99.8%) pressures of 8–11 MPa in copper-sealed home-built Inconel (Böhler L718V) autoclaves. SrD₂ was similarly obtained by annealing strontium ingots for 96 h at 675 K in 9 MPa D₂ atmosphere. La₂O₃ (R. Gerresheim Lübeck) was thermally treated prior to use for 6 h at 1425 K in an open corundum crucible in air and transferred while hot into the glovebox analogous to a literature procedure for Sm₂O₃.^[1] SrO was obtained by decomposition of SrCO₃ for 4 h at 1325 K in air.



LiLa₂NH₂O, LiLa₂ND₂O, and LiLa₂N_{1.5}D_{2.5} were obtained in two-step syntheses according to equations 1-4, adding the required amount of LaN and LaH₃ or LaD₃ in the second step to produce the K₂NiF₄ type phases. For the nitride hydride oxides, 5.47 g La₂O₃ and 1.28 g Li₃N (Aldrich, 99.5%; 1:2.2 molar ratio) were mixed and sealed in two stainless steel tubes. These were annealed at 1050 K for 12 h with a heating rate of 200 K h⁻¹ before switching off the furnace.^[2] Then, 2.41 g and 2.48 g of this sample were added to 2.02 g LaH₃ and 2.05 g LaD₃ respectively (0.1 molar excess of LaH₃/LaD₃), sealed in stainless steel tubes and annealed at 1050 K for 12 h with a heating rate of 25 K h⁻¹ before resuming to room temperature with 100 K h⁻¹. LiH and Li₂O were removed by stirring 2.40 g in 80 mL dry methanol (dried dynamically via 3 Å molar sieve)^[3] for 150 min, inert filtration, thrice flushing with 10 mL dry methanol each and subsequent vacuum drying.

For the synthesis of the nitride deuteride $\text{LiLa}_2\text{N}_{1.5}\text{D}_{2.5}$, 3.40 g LaD_3 and 842 mg Li_3N (1:1 molar ratio) were sealed in a stainless-steel tube and annealed at 1050 K for 4 h with a heating rate of 100 K h^{-1} before switching off the furnace. Then, 3.98 g of the product were added to 1.01 g LaD_3 (1:0.94 molar ratio $\text{LaN}:\text{LaD}_3$) and annealed in a stainless-steel tube at 1050 K for 8 h with a heating rate of 25 K h^{-1} before resuming to ambient temperature with 100 K h^{-1} . LiD was removed by distributing a 400 mg specimen on an inert fry before adding 5 mL deuterated methanol (Roth, 99.8 at.-% D) and slow filtration. The formation of gas bubbles, presumably D_2 , stopped after a few minutes. The sample was flushed thrice with totally 5 mL deuterated methanol and vacuum dried. $\text{LiLa}_2\text{N}_{1.5}\text{H}_{2.5}$ was obtained by an identical method using a smaller batch (128 mg LaH_3 , 473 mg LaN/LiH).

LiLa_2DO_3 and $\text{LiSrLaD}_2\text{O}_2$ were obtained from 54 mg LiD (abcr, 99%) and 1000 mg La_2O_3 resp. 70 mg LiD, 170 mg SrD_2 , 600 mg La_2O_3 and 192 mg SrO. The educts were sealed in stainless-steel tubes and annealed at 925 K for 12 h with a heating rate of 100 K h^{-1} .^[4,5] LiD was removed analogously to the procedure described above for $\text{LiLa}_2\text{N}_{1.5}\text{D}_{2.5}$.

Elemental Analysis

Hydrogen, nitrogen and, in case of $\text{LiLa}_2\text{NH}_2\text{O}$ oxygen, contents were measured by combustion and subsequent analysis of the gaseous products by Mikroanalytisches Labor Pascher (Remagen, Germany; washed $\text{LiLa}_2\text{NH}_2\text{O}$) or using a VARIO EL microanalyzer (Elementar Analysensysteme, Langenselbold, Germany; $\text{LiLa}_2\text{N}_{1.5}\text{H}_{2.5}$). The calculated values were corrected with the phase composition obtained by Rietveld analysis.

X-ray Powder Diffraction (XRPD)

XRPD samples were mixed with powdered diamond to reduce X-ray absorption and filled into glass capillaries of 0.5 mm diameter. The capillaries were previously stored at $170 \text{ }^\circ\text{C}$ for several days and transferred while hot into the glove box to reduce adsorbed water. The data were collected on a Stoe STADI-P diffractometer (Stoe, Darmstadt, Germany) with Ge(111) monochromatized $\text{Cu-}K_{\alpha 1}$ radiation in Debye-Scherrer geometry with a 0.5 mm diameter collimator. The Mythen 1K detector was moved in steps of $\Delta 2\theta = 3^\circ$ in the range $8^\circ \leq 2\theta \leq 89^\circ$ ($\text{LiLa}_2\text{NH}_2\text{O}$) resp. $8^\circ \leq 2\theta \leq 125^\circ$ ($\text{LiLa}_2\text{N}_{1.5}\text{H}_{2.5}$) with a collection time of 300 s ($\text{LiLa}_2\text{NH}_2\text{O}$) resp. 120 s ($\text{LiLa}_2\text{N}_{1.5}\text{H}_{2.5}$) per step. The procedure was repeated 6 ($\text{LiLa}_2\text{NH}_2\text{O}$) resp. 10 times ($\text{LiLa}_2\text{N}_{1.5}\text{H}_{2.5}$) and the individual datasets summed up to obtain the final diffraction pattern. The absence of the strongest Li_2O reflection peak in the washed $\text{LiLa}_2\text{NH}_2\text{O}$ sample was checked by measuring in the range $31^\circ \leq 2\theta \leq 37^\circ$, a collection time of 210 s per step and 4 repetitions added up. The diffraction geometry in addition to the high X-ray absorption of the sample result in the unusually high relative peak intensities at large diffraction angles.

Neutron Powder Diffraction (NPD)

Neutron powder diffraction data were collected at the HRPT high-resolution diffractometer at the Paul-Scherrer Institut (PSI) with a wavelength of 1.494 Å (LiLa₂NH₂O, LiLa₂ND₂O), and at the D20 high-resolution diffractometer at the Institute Laue-Langevin (ILL) with a wavelength of 1.865 Å (LiLa₂N_{1.5}D_{2.5}). Specimen were placed in indium sealed vanadium cylinders of 6 mm (LiLa₂NH₂O) or 8 mm diameter (LiLa₂ND₂O, LiLa₂N_{1.5}D_{2.5}) and measured at room temperature.

Rietveld Analysis

Crystal structures were refined based on powder diffraction data with the Rietveld method^[6] as implemented in the FullProf software version July 2017^[7] (neutron data). The background was simulated with polynomials of 2nd-3rd order and the reflection profiles by empirical pseudo-Voigt parameters. The zero-point error was refined in addition to the scaling factors, lattice, halfwidth (Caglioti formula), positional and thermal isotropic displacement parameters. For the NPD refinements, the asymmetry of the LiLa₂NH₂O reflections was refined with two asymmetry parameters for $2\theta \leq 20^\circ$, and for the XRPD measurements with one or two asymmetry parameters for $2\theta \leq 90^\circ$.

The distribution of the different anion species to the anionic sites in the NPD refinements of LiLa₂NH₂O and LiLa₂ND₂O was determined by a constrained refinement of their occupancy factors among both datasets with a weighing scheme of 1:1. This is necessary, as only a medium coherent scattering length \bar{b}_c can be refined per site n , which is calculated as the sum of the coherent scattering lengths of the individual species multiplied with their occupancy factors on this site (Equation 5 and 6), with H and D denoting the hydrogen and deuterium atoms.

$$\bar{b}_c(\text{site } n, \text{H}) = \text{SOF}(\text{N, site } n) b_c(\text{N}) + \text{SOF}(\text{O, site } n) b_c(\text{O}) + \text{SOF}(\text{H, site } n) b_c(\text{H}) \quad \text{Equation 5.}$$

$$\bar{b}_c(\text{site } n, \text{D}) = \text{SOF}(\text{N, site } n) b_c(\text{N}) + \text{SOF}(\text{O, site } n) b_c(\text{O}) + \text{SOF}(\text{D, site } n) b_c(\text{D}) \quad \text{Equation 6.}$$

A free refinement of the occupancy factors of all species is unstable, as they strongly correlate. By constraining those of hydrogen and deuterium atoms, i.e. $\text{SOF}(\text{H}, n) = \text{SOF}(\text{D}, n)$, the number of parameters is reduced. Furthermore, the sum of the occupancy factors of nitrogen and oxygen atoms is deducted from XRPD measurements and used as constraint, i.e. $\text{SOF}(\text{N}, n, \text{NPD}) + \text{SOF}(\text{O}, n, \text{NPD}) = \text{SOF}(\text{N} + \text{O}, n, \text{XRPD})$.

Subsequently, the constraint was lifted for the final structure refinement. The sum of nitrogen and oxygen atoms was set to 100% which agrees with the XRPD refinements. The composition of LiSrLaD₂O₂ was refined starting from the nominal sum formula with a charge constraint assuming full oxygen occupation of the 4e anionic site: $\Delta\text{SOF}(\text{La}) = \Delta\text{SOF}(\text{O}, 4c) = -\Delta\text{SOF}(\text{Sr})$.

Density Functional Theory (DFT) Calculations

The DFT calculations were performed with the Vienna ab initio simulation package (VASP)^[8] version 5.4.4, using the standard projector-augmented-wave pseudopotentials (PAW)^[9] from the VASP database (H, N, O, La), whereas that of lithium contained the s-level electrons of the first principal quantum number as semicore state (Li_sv). The exchange-correlation functional was described with the generalized gradient approximation (GGA) of Perdew, Burke and Ernzerhof.^[10] The Brillouin zone was integrated using the tetrahedron method with Blöchl corrections.^[11] The *k* grid was created automatically and Γ -centered, using a 10x10x4 grid for the structure optimizations and a 28x28x8 grid for the density of states (DOS) calculations. The cutoff energy was set to 800 eV and the structure optimizations were performed with full degrees of freedom regarding cell volume, cell shape and atomic positions using a conjugated gradient algorithm. Forces were converged to $10 \mu\text{eV}\text{\AA}^{-1}$ and electronic energies to 1 μeV . As the crystal structure of $\text{LiLa}_2\text{NH}_2\text{O}$ exhibits mixed N/O sites, the inversion center was removed to enable a simple treatment via DFT (t2 transition from *I4/mmm* to *I4mm*). The initial crystal structure parameters were obtained from this study ($\text{LiLa}_2\text{NH}_2\text{O}$, Table 1) and the literature (LiLa_2HO_3 *Immm*,^[4] ICSD collection code 8364). The DOS calculations were performed on fully relaxed structures with 1 meV energy resolution.

Impedance Spectroscopy

The preparation of specimen for impedance spectroscopy was complicated by both the air and temperature sensitivity of the nitride hydrides. This afforded an air-free atmosphere during measurement. Furthermore, a sintering of the samples was not possible, due to thermal decomposition at the required temperatures under formation of H_2 gas. Therefore, an air-tight commercial cell (KP Solid Cell, Hohsen Corp, Figure S1, left) was used to measure compressed samples. Washed $\text{LiLa}_2\text{NH}_2\text{O}$ was filled into the cell and densified by uni-axial cold pressing at 254 MPa (20 kN on $0,78 \text{ cm}^2$) within an argon filled glove box. The compressed powder was contacted by ion-blocking steel electrodes directly. The cell stack was placed in the air-tight cell housing. The stack was braced by tightly attaching a screw with a torque of 20 Nm. Impedance spectra were collected using a Biologic VMP 3 in a frequency range from 200 kHz to 100 mHz at ambient temperature (303 K).

For the temperature dependent measurements, a special measuring cell was constructed made of stainless steel and PVC (Figure S1, right). Washed $\text{LiLa}_2\text{NH}_2\text{O}$ specimen was filled into the cell which was subsequently contacted using silver paste and copper wires. Impedance spectra were recorded on an Impedance analyzer HP 4192A (Hewlett Packard) in a temperature range between room temperature and 150 °C using steps of 5 K and at frequencies ranging from 0.1 kHz to 10 MHz. The heating rate was 1 K/min and the applying voltage 0.5 V, respectively.

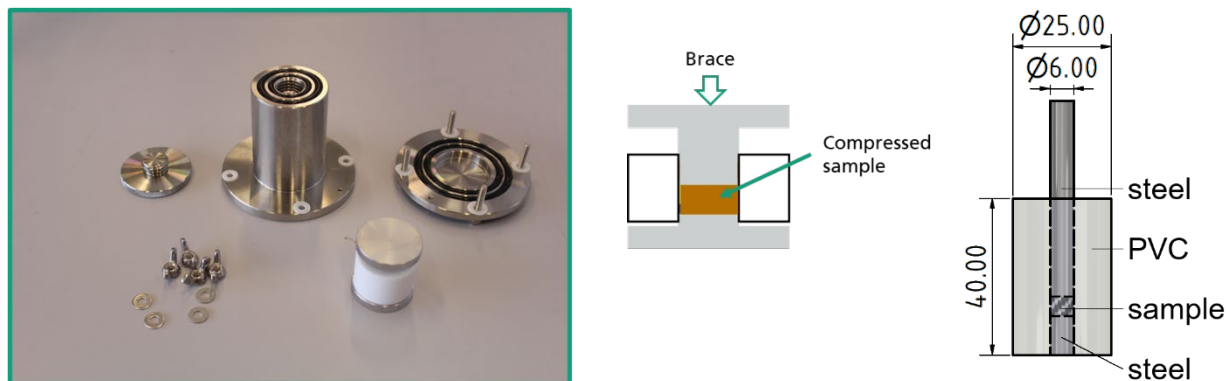


Figure S1. Inert measuring cells for impedance spectroscopy. Left: Commercial KP Solid Cell (Hohsen corp.) for electrochemical testing of cold-compressed samples; right: custom-made inert measuring cell for non-compacted powdered samples.

Nuclear Magnetic Resonance (NMR) Spectroscopy.

Washed $\text{LiLa}_2\text{ND}_2\text{O}$ and $\text{LiLa}_2\text{N}_{1.5}\text{D}_{2.5}$ were mixed with dry La_2O_3 in 1:10 mass ratio and filled into ZrO_2 cylinders. Solid-state NMR experiments were carried out with a Bruker Avance 400 spectrometer at a magnetic field strength of 9.4 T. A two-channel 4 mm MAS probe was used both at static and MAS conditions and different spinning frequencies. NMR frequencies were 400.167 MHz for ^1H ($I = 1/2$), 61.428 MHz for ^2H ($I = 1$) and 155.52 MHz for ^7Li ($I = 3/2$). A standard one-pulse sequence and a Hahn-echo sequence were used for MAS and static measurements, respectively. Typical pulse lengths were 1 μs (short flip angle in single pulse experiments) or 5 μs ($\pi/2$ pulse in echo sequence) and recycle delays 60 s. Spectral deconvolution was done using the dmfit program.^[12]

The solid-state NMR data are analyzed with regard to dipolar and quadrupolar coupling. The expected dipolar coupling was calculated based on the second moment^[13] approach by taking the distances to other NMR-active nuclei from the refined crystal structure. From the second moment the Gaussian linewidth was calculated.^[14] The quadrupolar coupling was calculated by a simple point-charge model by the surrounding ions and their relative distance to the nuclear spin under observation.^[15] For this, also different scenarios were analyzed based on the non-uniform site occupation factors obtained from NPD analysis. Temperature-dependent measurements were performed for $\text{LiLa}_2\text{ND}_2\text{O}$ down to 210 K.

Results and Discussion

LiLa₂NH₂O and LiLa₂ND₂O

Synthesis and XRPD Analysis

From the reaction of La₂O₃ and Li₃N, a mixture of LaN and Li₂O was obtained. A dark grey powder was formed from its reaction with LaH₃, whose X-ray diffraction pattern resembled that of LiLa₂HO₃ with additional reflections from residual Li₂O and small amounts of LaN. Indexing the major phase produced good results for space group *I4/mmm* and lattice parameters $a = 3.65 \text{ \AA}$ and $c = 13.36 \text{ \AA}$, a combination which is commonly found for K₂NiF₄ type compounds (a and c in \AA for LiLa₂HO₃: 3.66, 13.14;^[16] LiSr₂NH₂: 3.81, 13.72).^[17] A Rietveld refinement starting from the LiLa₂HO₃ structure model yielded a good correspondence between measured and calculated data. As the X-ray scattering contrast between nitrogen and oxygen is very small, only the sum of their site occupancy factors *SOF* can be significantly refined in the crystal structure, while hydrogen is quasi-invisible due to its very small contribution to the diffraction pattern. The refinement of *SOF*(N+O) on both anion sites resulted in a full occupation of the 4e site and an empty 4c site. As the sample furthermore contained no other N-containing phases (except ~2 wt.-% LaN), the majority of nitrogen from the educt mixture must thus be found in this new compound. Both factors indicate a sum formula LiLa₂NH₂O, which was confirmed by elemental analysis (see the next subsection).

In one of our batches, we observed tetragonal LaHO^[18] as secondary phase. The reaction pathway might thus involve its formation from LaH₃ and Li₂O with subsequent reaction with LaN: $\text{Li}_2\text{O} + \text{LaH}_3 \rightarrow 2 \text{LiH} + \text{LaHO}$, $\text{LiH} + \text{LaHO} + \text{LaN} \rightarrow \text{LiLa}_2\text{NH}_2\text{O}$. As the annealing temperature is higher than the melting point of LiH (1050 K > 966 K),^[19] a crystallization of LiLa₂NH₂O from a LiH melt after formation of the latter from Li₂O and LaH₃ instead of a solid-solid reaction is plausible. The reactivity of molten LiH is an often-observed concept in the synthesis of heteroanionic hydrides, e.g. for LiLa₂HO₃^[20] or LiSr₂SiO₄H.^[21] For the formation of isotypical LiNd₂HO₃ from LiCl salt fluxes it was however reported, that the formation of the hydride oxide occurs only below the melting point of the flux agent due to its thermal instability.^[22] LiH might thus also promote the formation of LiLa₂NH₂O below its melting point. A mixture of LiH, LaH₃, La₂O₃ and LaN from ball milling in an autoclave at 820 K did however not result in a chemical reaction.^[23] The energy gain from the initial metathesis reaction of Li₂O and LaH₃ might therefore be an important factor for a successful synthesis.

The coupling product Li₂O and minor amounts of LiH (see also Figure 1 in main text) could be removed by inert washing in dry methanol. LiH was directly protolyzed by contact with methanol as observed by the formation of gaseous H₂, and the removal of Li₂O was confirmed by the absence of its strongest reflection peak in the XRPD pattern (111 at $Q = 2.359 \text{ \AA}^{-1}$). The washed

sample had a dark brown color and the crystallographic and microstructural characteristics of the major phase did not change significantly, ergo it was not affected by washing (Figure S2).

Upon contact with air, $\text{LiLa}_2\text{NH}_2\text{O}$ hydrolyzes within minutes to form $\text{La}(\text{OH})_3$, Li_2O and NH_3 .

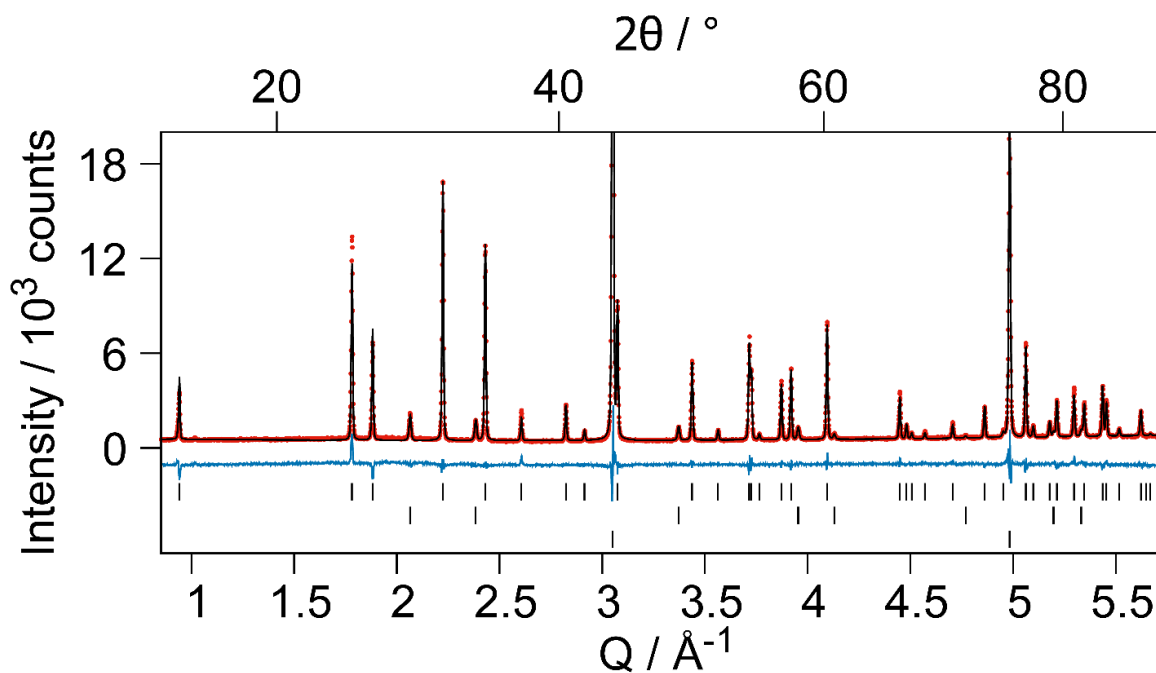


Figure S2. Rietveld refinement of the crystal structure of washed $\text{LiLa}_2\text{NH}_2\text{O}$ based on XRPD data at ambient temperature (Stoe STADI-P, λ : $\text{Cu-K}\alpha_1$; $R_{\text{wp}} = 7.8\%$, $GoF = 2.5$). Bragg markers denote from top to bottom: $\text{LiLa}_2\text{NH}_2\text{O}$ ($I4/mmm$, 93.0(6) wt.-%, $a = 3.65441(3)$ Å, $c = 13.34805(16)$ Å), LaN ($Fm\bar{3}m$, 6.8(3) wt.-%, $a = 5.26872(17)$ Å), diamond (added to reduce X-ray absorption, not regarded in phase ratios). Red dots: measurement *meas*, black curve: calculation *calc*, blue curve: difference *meas-calc*.

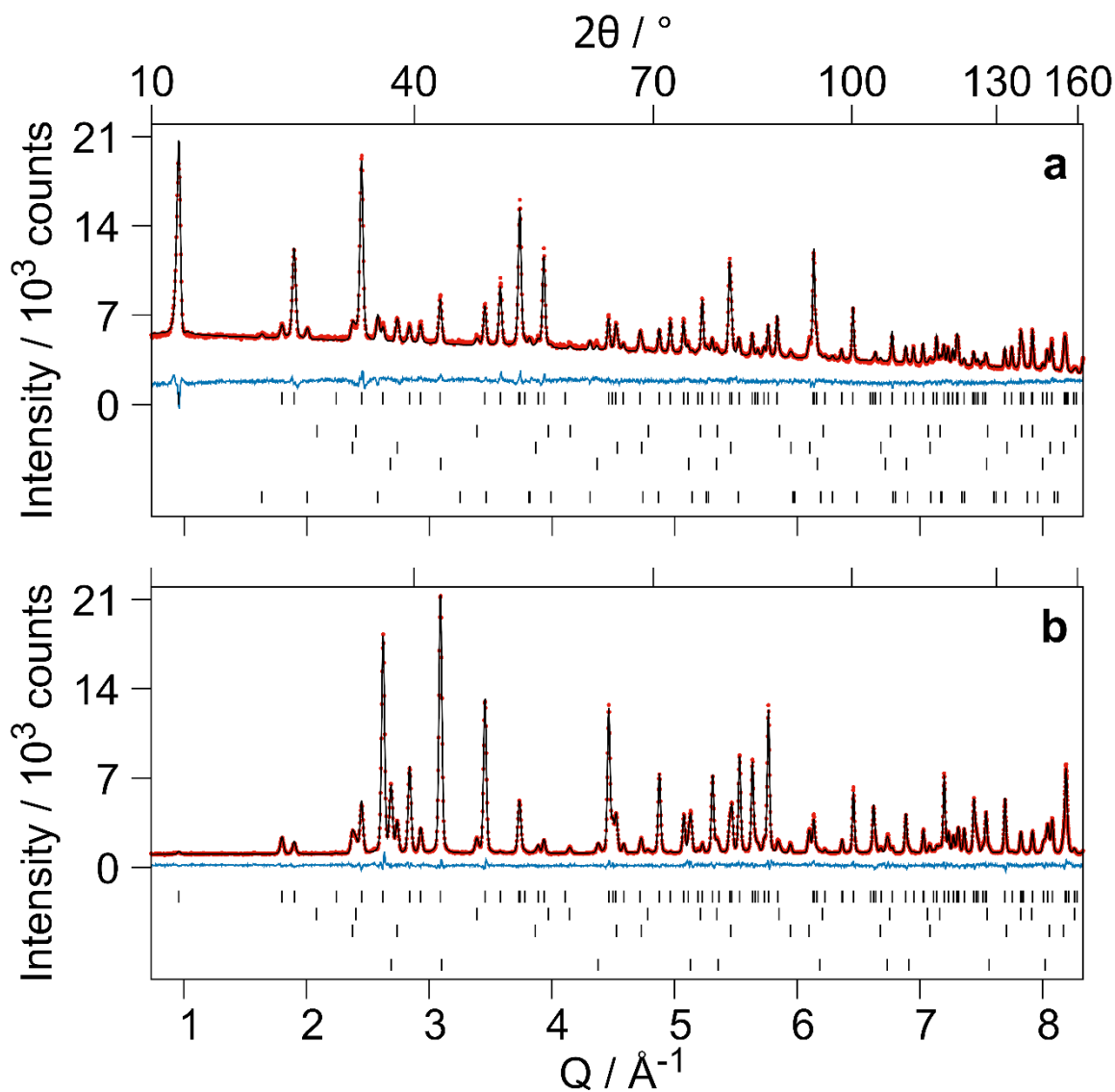


Figure S3. Rietveld refinement of the crystal structures of $\text{LiLa}_2\text{N}_{0.84(6)}\text{H}_{1.56(3)}\text{O}_{1.16(6)}$ (top, **a**) and $\text{LiLa}_2\text{N}_{0.85(3)}\text{D}_{1.898(14)}\text{O}_{1.15(3)}$ (bottom, **b**) based on neutron diffraction data at ambient temperature (HRPT diffractometer, $\lambda = 1.494 \text{ \AA}$). **a:** $R_{\text{wp}} = 3.1\%$, $\text{GoF} = 2.1$. Bragg markers denote from top to bottom: $\text{LiLa}_2\text{N}_{0.84(6)}\text{H}_{1.56(3)}\text{O}_{1.16(6)}$ ($I4/mmm$, 93(2) wt.-%, $R_1 = 10.5\%$, $a = 3.65740(6) \text{ \AA}$, $c = 13.3679(4) \text{ \AA}$), LaN ($Fm\bar{3}m$, 1.74(15) wt.-%, $a = 5.2695(15) \text{ \AA}$), Li_2O ($Fm\bar{3}m$, 3.39(12) wt.-%, $a = 4.6155(4) \text{ \AA}$), LiH ($Fm\bar{3}m$, 0.23(3) wt.-%, $a = 4.0855(9) \text{ \AA}$), Li_3N ($P6/mmm$, 1.61(8) wt.-%, $a = 3.6490(6) \text{ \AA}$, $c = 3.8836(12) \text{ \AA}$). **b:** $R_{\text{wp}} = 4.0\%$, $\text{GoF} = 1.8$. Bragg markers denote from top to bottom: $\text{LiLa}_2\text{N}_{0.85(3)}\text{D}_{1.898(14)}\text{O}_{1.15(3)}$ ($I4/mmm$, 91.9(11) wt.-%, $R_1 = 3.1\%$, $a = 3.65603(4) \text{ \AA}$, $c = 13.3557(2) \text{ \AA}$), LaN ($Fm\bar{3}m$, 3.11(12) wt.-%, $a = 5.2721(5) \text{ \AA}$), Li_2O ($Fm\bar{3}m$, 3.48(9) wt.-%, $a = 4.61823(18) \text{ \AA}$), LiD ($Fm\bar{3}m$, 1.56(3) wt.-%, $a = 4.07385(16) \text{ \AA}$). Red dots: measurement *meas*, black curve: calculation *calc*, blue curve: difference *meas-calc*. The difference curve in **a** is offset by $15 \cdot 10^2$ counts.

Crystal Structure Analysis

To analyze the anion ordering, neutron diffraction data were collected on $\text{LiLa}_2\text{NH}_2\text{O}$ and a deuterated specimen $\text{LiLa}_2\text{ND}_2\text{O}$. By utilizing the isotopic sensitivity of neutrons, a more detailed picture of the hydrogen substructure can be obtained (bound coherent neutron scattering lengths in fm: N 9.4, H -3.7, D 6.7, O 5.8).^[24] The constrained refinement confirmed the K_2NiF_4 structure type with nitrogen and oxygen atoms occupying the La-rich apical 4e site in a disordered fashion, and hydrogen (deuterium) atoms found on the Li-rich equatorial site 4c with a small number of vacancies (Tables 1 and S1, Figures 1, 2, S3). Such vacancies were already reported for e.g. $\text{LiSr}_{1.3}\text{La}_{0.7}\text{H}_{1.7}\text{O}_2$.^[16] The amount of nitrogen or oxygen atoms on the 4c site is negligible, as is the amount of hydrogen atoms on the 4e site. Here, the ratio of nitrogen and oxygen atoms differs slightly but significantly from 1:1 with a surplus of oxygen atoms. There is furthermore no significant scattering contribution on the interstitial site 4d, and we did not observe a underoccupation of the lithium site, which was previously reported for some hydride oxides.^[20] The resultant sum formula differs from that proposed above and is slightly poorer in nitrogen and hydrogen, somewhat richer in oxygen, and slightly charge-imbalanced (+0.60(14)): $\text{LiLa}_2\text{N}_{0.84(6)}\text{H}_{1.56(3)}\text{O}_{1.16(6)}$ and $\text{LiLa}_2\text{N}_{0.85(3)}\text{D}_{1.898(14)}\text{O}_{1.15(3)}$. These compositions were confirmed by elemental analysis on washed $\text{LiLa}_2\text{NH}_2\text{O}$ (N: 3.8(2) wt.-%, calc: 3.7 wt.-%; H: 0.69(5) wt.-%, calc: 0.50 wt.-%; O: 5.9(2) wt.-%, calc: 5.9 wt.-%; accounting for 2% LaN content). A charge-balanced model showed large deviations from the experimentally determined nitrogen and oxygen contents (N: 5.8 wt.-%; O: 3.5 wt.-%). Furthermore, the resulting compositions of hydride $\text{LiLa}_2\text{N}_{1.31(2)}\text{H}_{1.69(2)}\text{O}_{0.69(2)}$ and deuteride $\text{LiLa}_2\text{N}_{1.05(1)}\text{D}_{1.95(1)}\text{O}_{0.95(1)}$ varied strongly. Regarding identical synthesis conditions and phase compositions of the product, this is unlikely. Therefore, the charge-imbalanced structure models yielding compositions $\text{LiLa}_2\text{N}_{0.84(6)}\text{H}_{1.56(3)}\text{O}_{1.16(6)}$ and $\text{LiLa}_2\text{N}_{0.85(3)}\text{D}_{1.898(14)}\text{O}_{1.15(3)}$ better explain the experimental findings.

Table S1. Atomic distances up to 3 Å in $\text{LiLa}_2\text{N}_{0.84(6)}\text{H}_{1.56(3)}\text{O}_{1.16(6)}$ ^[a] (H) and $\text{LiLa}_2\text{N}_{0.85(3)}\text{D}_{1.898(14)}\text{O}_{1.15(3)}$ ^[b] (D) from NPD data at room temperature.

Atom 1	Atom 2	quantity	Distance / Å	
			H	D
Li	N/O	2	2.3053(16)	2.3093(9)
	H/D	4	1.82870(3)	1.828015(20)
La	N/O	1	2.425(2)	2.4195(13)
		4	2.6099(3)	2.61020(18)
	H/D	4	2.6763(9)	2.6721(7)
N/O	H/D	4	2.9425(13)	2.9453(7)
H/D	H/D	4	2.58617(4)	2.58520(3)

LiLa₂N_{1.5}H_{2.5} and LiLa₂N_{1.5}D_{2.5}

Synthesis and XRPD Analysis

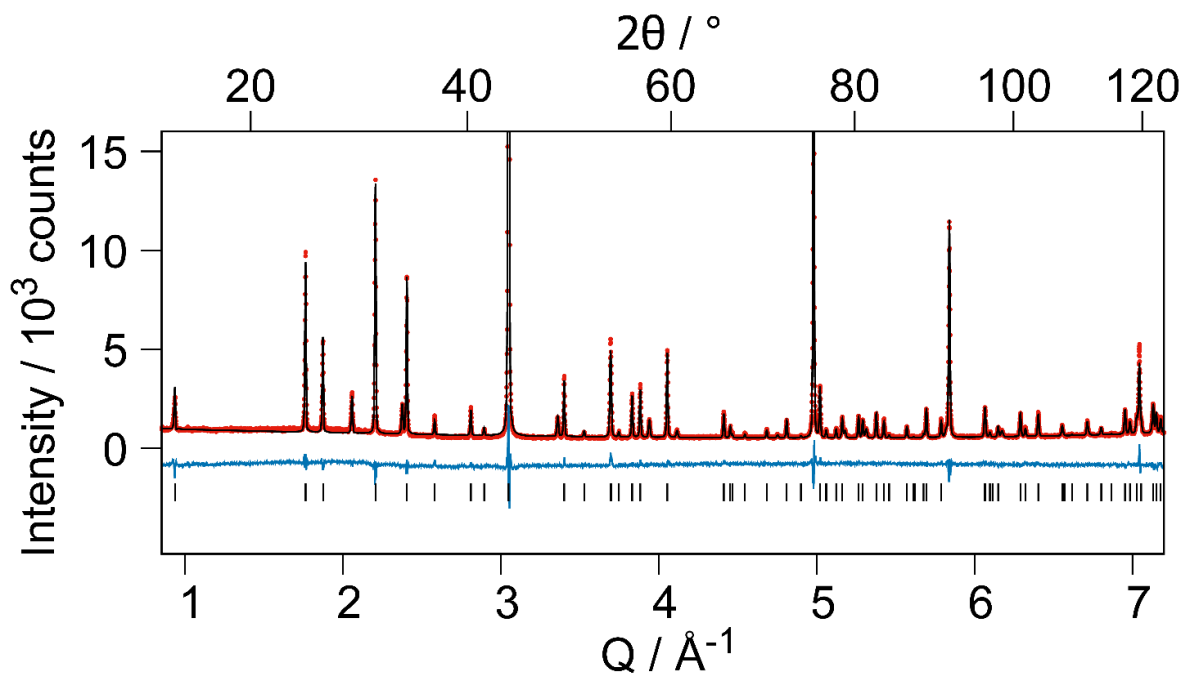


Figure S4. Rietveld refinement of the crystal structure of washed LiLa₂N_{1.5}D_{2.5} based on XRPD data at ambient temperature (Stoe STADI-P, λ : Cu-K α 1; R_{wp} = 8.0%, GoF = 2.5). Bragg markers denote from top to bottom: LiLa₂N_{1.5}D_{2.5} ($I4/mmm$, 90.1(7) wt.-%, a = 3.69385(4) Å, c = 13.41098(18) Å), LaN ($Fm\bar{3}m$, 9.9(3) wt.-%, a = 5.28694(13) Å), diamond (added to reduce X-ray absorption, not regarded in phase analysis). Red dots: measurement *meas*, black curve: calculation *calc*, blue curve: difference *meas-calc*.

The reaction of LaH₃ and Li₃N produced LaN and LiH in addition to a small proportion of a phase with K₂NiF₄ type reflection pattern with from LiLa₂NH₂O distinct lattice parameters (a = 3.69352(5) Å, c = 13.4278(2) Å). The content of the latter increased after adding LaH₃ and subsequent annealing (Figure S3). Its structure could be refined starting from the structure model of LiLa₂NH₂O and produced a good fit for a mainly nitrogen-filled 4e site ($SOF(N)$ = 0.69(4)) and an empty 4c site ($SOF(N)$ = 0.00(5)), which agrees with the results of the elemental analysis (N: 6.9(4) wt.-%, calc.: 6.4 wt.-%; H: 1.07(2) wt.-%, calc.: 1.6 wt.-%, considering LaN, Li₃N and LiH content¹). LiD

¹ The employed method was calibrated for organic substances with substantially higher hydrogen weight content. Results for small hydrogen contents like here are therefore less accurate and should be regarded as semi-quantitative.

could be removed from a deuterated sample by inert washing in dry methanol-d4, as evidenced by the declining formation of D₂. Alike LiLa₂NH₂O, LiLa₂N_{1.5}H_{2.5} is very air sensitive and quickly hydrolyzes to form La(OH)₃, Li₂O and NH₃.

Crystal Structure Analysis

The neutron powder diffraction analysis on a deuterated sample confirmed the K₂NiF₄-type structure model (Figure S4). The amount of vacancies on the 4c site is insignificant (*SOF*(D, 4c) = 1.000(9)), as is the charge-imbalance of the resultant sum formula LiLa₂N_{1.58(6)}D_{2.41(6)} (-0.2(5)). The interstitial 4d site is not significantly occupied (*SOF*(D, 4d) = -0.006(4)).

Table S2. The crystal structure parameters of LiLa₂N_{1.58(6)}D_{2.41(6)}^[a] obtained from NPD analysis at room temperature.

Atom	Wyck.	x	y	z	<i>SOF</i>	<i>B</i> _{iso} / Å ²
Li	2a	0	0	0	1	0.79(16)
La	4e	0	0	0.35525(9)	1	0.19(4)
N	4e	0	0	0.17368(8)	0.79(3)	0.59(5)
D1	4e	0	0	z(N)	1- <i>SOF</i> (N)	<i>B</i> _{iso} (N)
D2	4c	0	1/2	0	1	1.19(5)

[a] *I4/mmm*, *a* = 3.69326(8) Å, *c* = 13.4133(3) Å.

Table S3. Atomic distances in LiLa₂N_{1.58(6)}D_{2.41(6)} up to 3 Å based on NPD data at room temperature.

Atom 1	Atom 2	quantity	Distance / Å
Li	N/D1	2	2.3296(11)
	D2	4	1.84663(4)
La	N/D1	1	2.4355(16)
		4	2.6402(2)
	D2	4	2.6795(9)
N/D1	D2	4	2.9727(8)
D2	D2	4	2.61153(6)

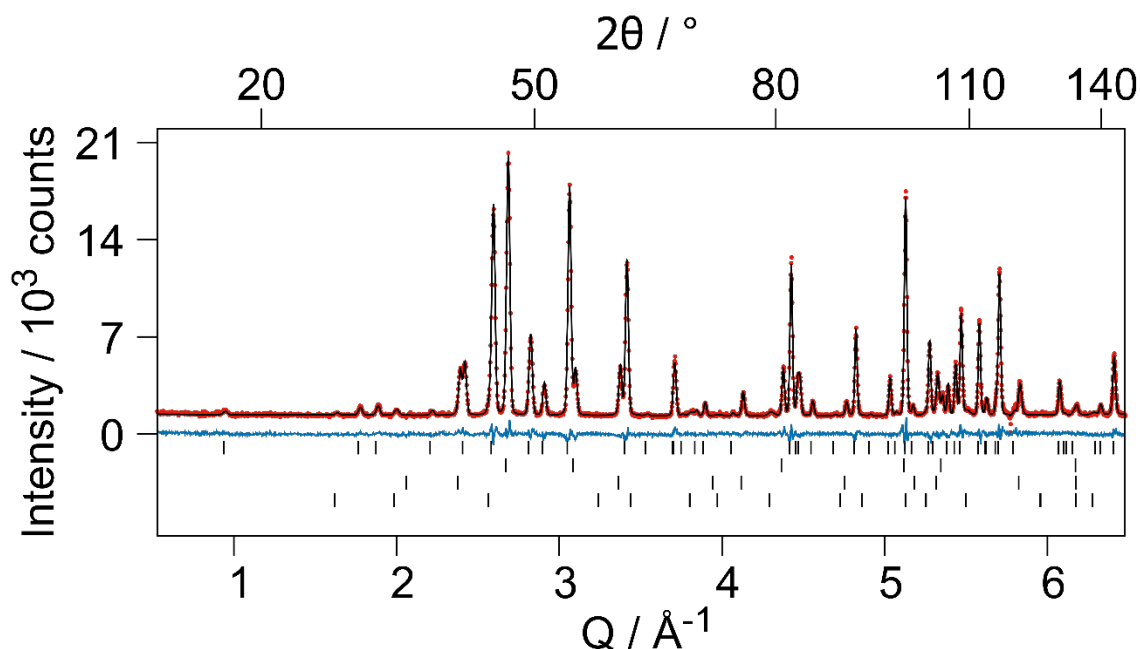


Figure S5. Rietveld refinement of the crystal structure of $\text{LiLa}_2\text{N}_{1.58(6)}\text{D}_{2.41(6)}$ based on neutron diffraction data at ambient temperature (D20 diffractometer, $\lambda = 1.865 \text{ \AA}$, $R_{\text{wp}} = 5.1\%$, $\text{GoF} = 1.9$). Bragg markers denote from top to bottom: $\text{LiLa}_2\text{N}_{1.58(6)}\text{D}_{2.41(6)}$ ($I4/mmm$, 81.4(10) wt.-%, $R_I = 4.1\%$, $a = 3.69326(8) \text{ \AA}$, $c = 13.4133(3) \text{ \AA}$), LiD ($Fm\bar{3}m$, 7.09(10) wt.-%, $a = 4.07201(11) \text{ \AA}$), LaN ($Fm\bar{3}m$, 10.3(3) wt.-%, $a = 5.28575(17) \text{ \AA}$), Li_3N ($P6/mmm$, 1.17(7) wt.-%, $a = 3.6533(10) \text{ \AA}$, $c = 3.8776(21) \text{ \AA}$). Red dots: measurement *meas*, black curve: calculation *calc*, blue curve: difference *meas-calc*. The data points from $117.75\text{--}118.05^\circ 2\theta$ were excluded due to a detector error.

Crystal Structure Discussion

The Li-H, Li-D, Li-N, and Li-O distances in $\text{LiLa}_2\text{N}_{0.85(3)}\text{H}_{1.854(12)}\text{O}_{1.15(3)}$, $\text{LiLa}_2\text{N}_{0.85(3)}\text{D}_{1.854(12)}\text{O}_{1.15(3)}$, and $\text{LiLa}_2\text{N}_{1.58(6)}\text{D}_{2.41(6)}$ are similar to those in LiLa_2HO_3 and LiLa_2DO_3 (Li-H: 1.78 \AA , 1.79 \AA ; Li-O: 2.29 \AA)^[4,20] and smaller than those in Li_4NH (Li-H: 1.95 \AA , 2.59 \AA ; Li-N: 2.07 \AA)^[25] and most binary compounds (LiH, LiD: 2.03 \AA , 2.04 \AA ;^[26] Li_3N : 1.94 – 2.1, 2.32 \AA ;^[27] Li_2O : 2.00 \AA)^[28] In comparison with LiSr_2NH_2 , the Li-H distances resemble those in the orthorhombic compound (1.88 \AA)^[29] and are larger than in the isotypical tetragonal one (1.91 \AA)^[17] while the opposite is true for the Li-N distance (orthorhombic: 2.08 \AA ;^[29] tetragonal: 2.29 \AA)^[17]

The La-H distances are larger than usually observed for heteroanionic hydrides (LaHO: 2.42 \AA , 2.51 \AA , 2.72 \AA ;^[18] LiLa_2HO_3 , LiLa_2DO_3 : 2.58 \AA)^[4,20] but are still within the upper range of La-H distances in binary and multinary compounds ($\text{LaD}_{2.5}$: 2.41 – 2.86 \AA ;^[30] LaH_3 : 2.81 \AA)^[31] There are four larger La-N/O distances and a shorter one. While the larger ones resemble those observed in LiLa_2HO_3 (2.42 \AA , 2.43 \AA , and 2.64 \AA , 2.65 \AA)^[4,20] as well as LaN (2.64 \AA)^[2] the shorter one is similar to A-type La_2O_3 (2.37 \AA , 2.46 \AA)^[32] Superstructure reflections as expected in the

case of an ordering of nitrogen and oxygen atoms to individual sites like $I4/mmm \rightarrow P4/mmm$ were however not observed.

The isotropic Debye-Waller factors are similar to those in other heteroanionic hydrides ($B_{\text{iso}}(\text{Li})$: 0.7 - 1.2 \AA^2 ;[4,17,20,29,33] $B_{\text{iso}}(\text{La})$: 0.4–0.6 \AA^2 ;[4,18,20] $B_{\text{iso}}(\text{N})$: 0.5-0.8 \AA^2 ;[17,25,29] $B_{\text{iso}}(\text{O})$: 0.4–0.7 \AA^2 ;[4,18,20] $B_{\text{iso}}(\text{H})$: 1.66 \AA^2 ;[4] $B_{\text{iso}}(\text{D})$: 1.52 \AA^2).[20] The increased mass of the deuterium isotope results in a smaller vibrational amplitude compared to protium, which is expressed in its smaller B_{iso} values and unit cell volumes (isotope effect).[34]

LiLa₂DO₃ and LiSrLaD₂O₂

Both LiLa₂DO₃ and LiSrLaD₂O₂ were obtained as single phase gray powders (Figures S6, S7).

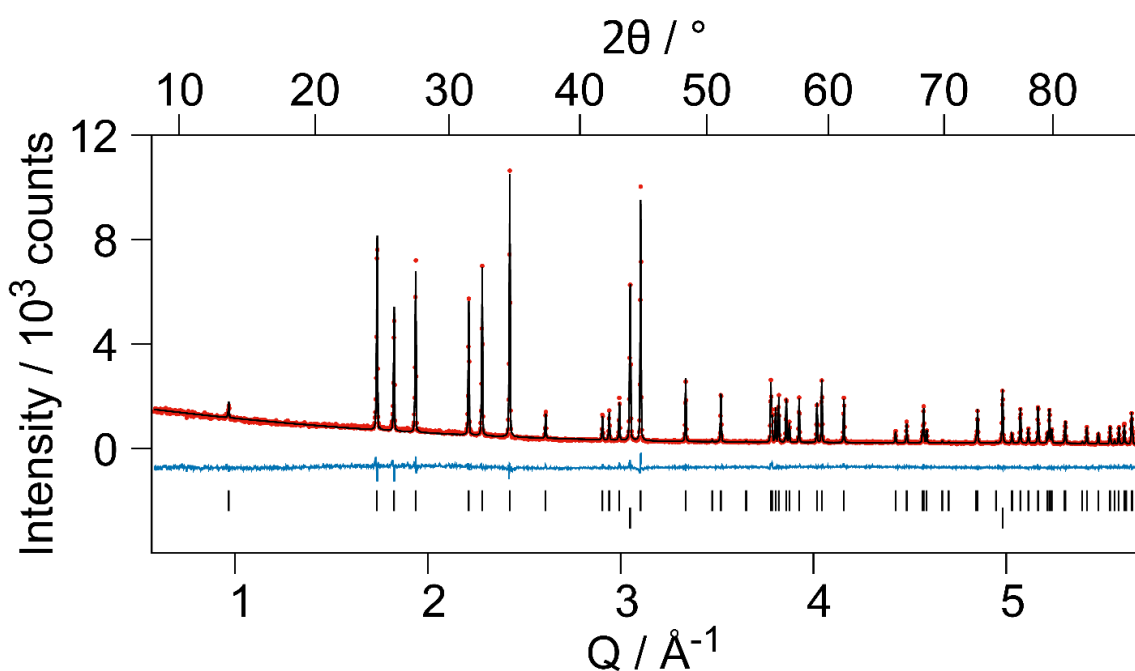


Figure S6. Rietveld refinement of the crystal structure of washed LiLa₂DO₃ based on XRPD data at ambient temperature (Stoe STADI-P, λ : Cu- $K_{\alpha 1}$; $R_{\text{wp}} = 7.4\%$, $GoF = 2.8$). Bragg markers denote from top to bottom: LiLa₂DO₃ ($Immm$, 100 wt.-%, $a = 3.56801(6)$ \AA , $b = 3.76345(6)$ \AA , $c = 12.9651(2)$ \AA), diamond (added to reduce X-ray absorption, not regarded in phase analysis). Red dots: measurement *meas*, black curve: calculation *calc*, blue curve: difference *meas-calc*.

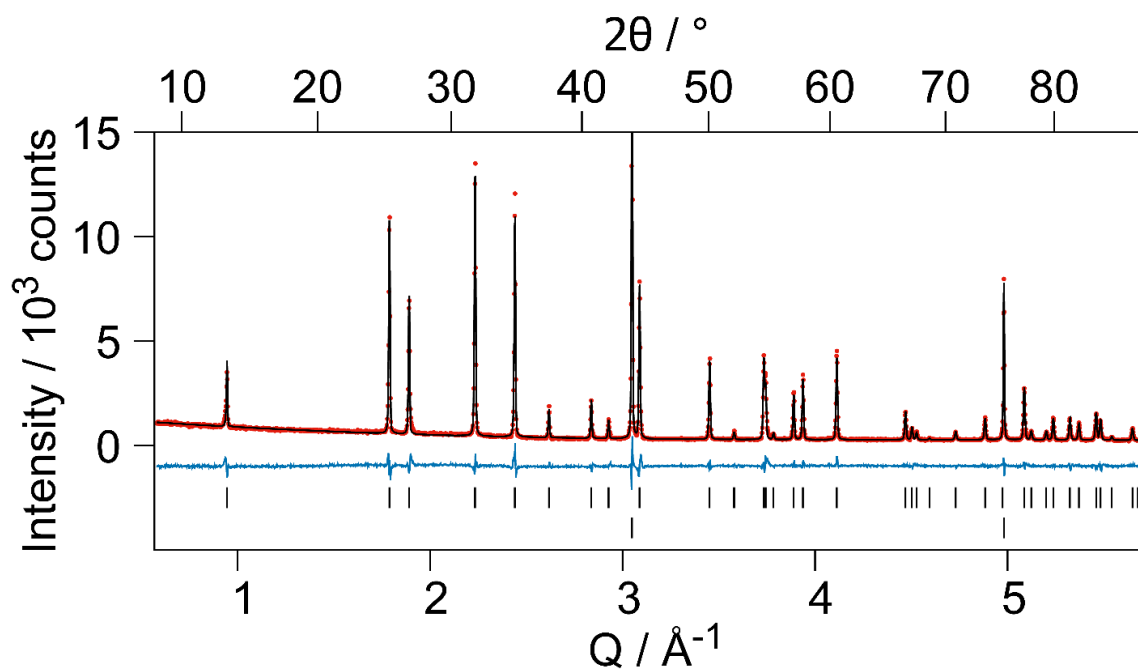


Figure S7. Rietveld refinement of the crystal structure of washed $\text{LiSrLaD}_2\text{O}_2$ based on XRPD data at ambient temperature (Stoe STADI-P, λ : $\text{Cu-K}\alpha_1$; $R_{\text{wp}} = 8.9\%$, $GoF = 2.3$). Bragg markers denote from top to bottom: $\text{LiSr}_{0.392(8)}\text{La}_{0.608(8)}\text{D}_2\text{O}_{2.104(8)}$ ($I4/mmm$, 100 wt.-%, $a = 3.63711(5)$ \AA , $c = 13.2741(2)$ \AA), diamond (added to reduce X-ray absorption, not regarded in phase analysis). Red dots: measurement *meas*, black curve: calculation *calc*, blue curve: difference *meas-calc*.

Density of States (DOS)

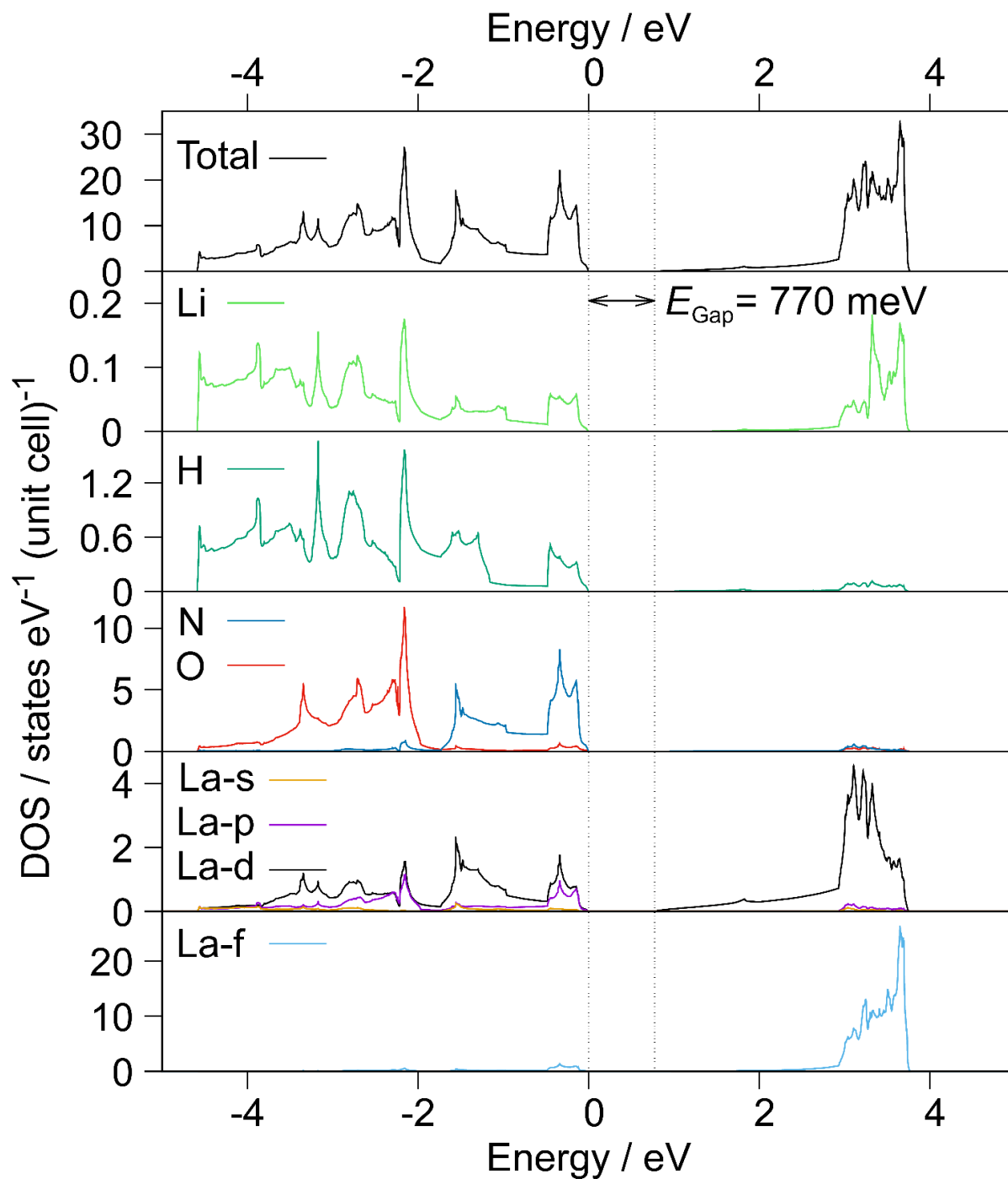


Figure S8. Total and projected DOS for ordered $\text{LiLa}_2\text{NH}_2\text{O}$ ($I4mm$) from DFT calculations. Please note the different y-scaling of the single graphs.

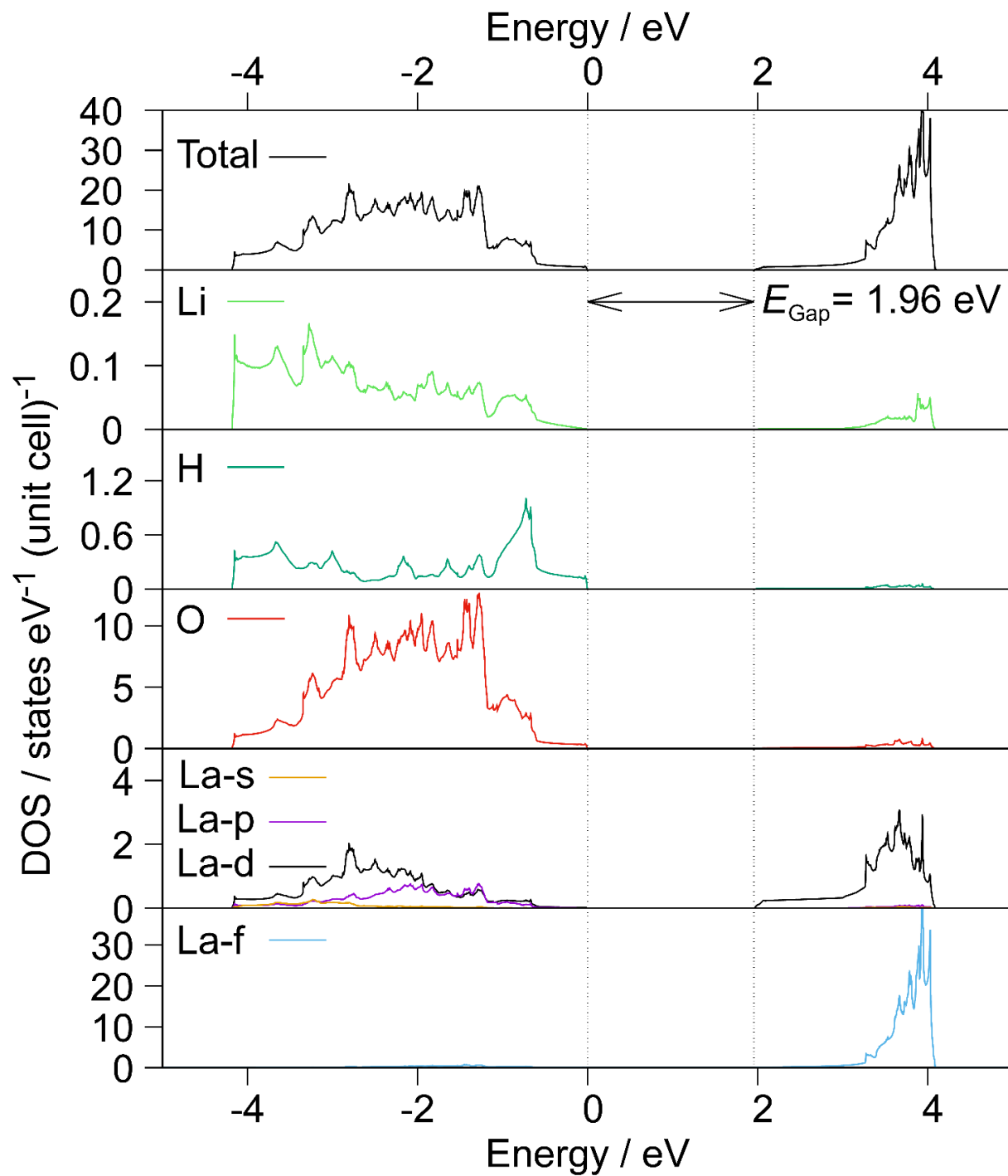


Figure S9. Total and projected DOS of LiLa_2HO_3 ($Im\bar{m}m$) from DFT calculations. Mind the different y-scaling of the individual graphs.

Impedance Spectroscopy

To investigate the effect of the formal aliovalent anion substitution on the conductivity of the samples, impedance spectra of several washed $\text{LiLa}_2\text{NH}_2\text{O}$ powder samples were measured in air-tight sample cells both at room temperature (cold-densified samples) and in a temperature range between room temperature and $150\text{ }^\circ\text{C}$ (non-compacted samples). XRD investigations after impedance spectroscopy confirmed that no decomposition or oxidation of the samples occurred during the electrical measurements. It should be noted the powder samples that were not compacted or sintered exhibit lower signal-to-noise ratios at low frequencies ($f < 1\text{ kHz}$). The calculated electrical conductivities of the non-compacted samples are still rather low at room temperature ($\sigma \leq 10^{-8}\text{ S/cm}$). In contrast, cold densified pellets showed a much better particle contact. The Bode-plot is given in Fig S10, left. Measurements with ion-blocking electrodes showed a conducting behavior in the low-frequency range without a polarization effect due to blocking electrodes. Thus, in the DC-limit at low frequencies electron conduction is observed. The Bode-plot furthermore shows a pure ohmic behavior at low frequencies with a phase angle $\varphi = 0^\circ$.

The highest obtained electron conductivity (σ_e) value is $3.5 \cdot 10^{-3}\text{ S cm}^{-1}$. Due to the sinter-free contacting, electron conduction is limited by grain boundaries and a constriction resistance. The data can be fitted by a simple R-Q circuit (R = capacitor, Q = constant phase element) and the capacitance can be estimated from fitting parameters by $C = QR^{1/\alpha} R^{-1}$. The capacitance of $2.7 \cdot 10^{-11}\text{ F cm}^{-1}$ is a typical value for grain boundaries dominated conduction. The low capacitance furthermore can be attributed to insufficiently connected particles.^[35] Since densification was achieved at higher pressures than the bracing of the cell, conductivity decreases with time (Figure S10, right) but can be restored by subsequent compression.

For the non-compacted samples, the impedance spectra could be evaluated using the simple model of a lossy capacitor, which is commonly used describing insulating samples like e. g. BaTiO_3 or CaTaO_2N ceramics.^[36] As a result, the real part of complex permittivities (ϵ') and dissipation factors ($\tan \delta$) can be calculated which are shown in Fig. S11 and Fig. S12.

The real part of permittivities are nearly frequency independent (Fig. S12) and are slightly decreasing from room temperature ($\epsilon' = 14$) to $74\text{ }^\circ\text{C}$ ($\epsilon' = 8$). At elevated temperatures, the permittivity increases but becomes frequency dependent and correlates with higher dielectric losses (Fig. S12). The loss tangent values, which are linked with the conductivity of the sample, are rather low below a temperature of roughly $100\text{ }^\circ\text{C}$ and increase at higher temperatures indicating semiconducting behavior of $\text{LiLa}_2\text{NH}_2\text{O}$.

Due to the structural relationship with recently discovered hydride ion conductors that all crystallize in the K_2NiF_4 -type or varieties thereof,^[16,37,38] it is plausible that $\text{LiLa}_2\text{NH}_2\text{O}$ shows hydride ion conductivity, too. From the current measurement setup, it is however not possible to characterize ionic conductivity independently from electron conduction. This required either a setup with electron blocking and ion conducting electrodes under the aid of a pure hydride-ion conductor, e.g. a symmetrical chain like

TiH₂/Ti | K₂NiF₄-type H⁻-ion conductor | LiLa₂NH₂O | K₂NiF₄-type H⁻-ion conductor | Ti/TiH₂

A second approach might be the determination of hydride transport in a hydride battery-like cell, e.g.

MH_x | LiLa₂NH₂O / M'

with $MH_x + M' \rightarrow M + M'H_x$ being an exergonic reaction. Due to the assumed mixed conductivity (electrons and H⁻ ions), such a cell is internally short circuited and will discharge. The hydride transport can be verified by the formation of $M'H_x$, e.g. by XRPD. Possible pairs might be transition metals like Pd/PdH_x or Ti/TiH_x. These investigations are beyond the scope of this work, thus, hydride conduction in LiLa₂NH₂O stays elusive.

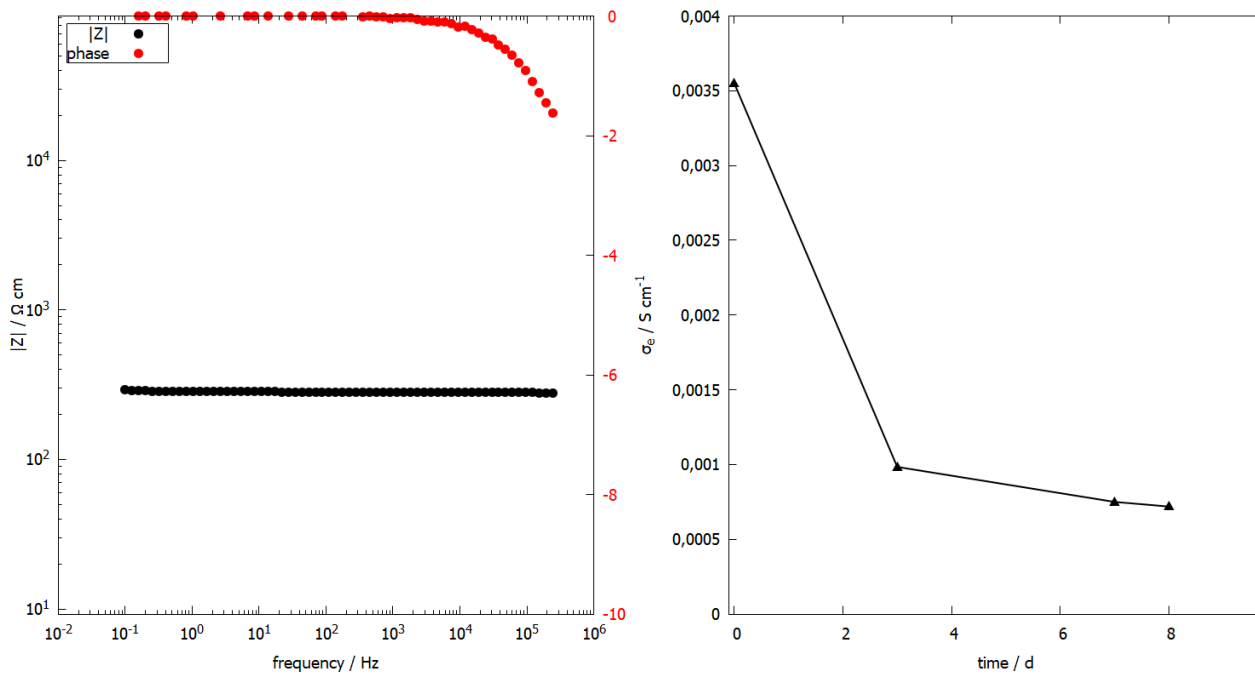


Figure S10. Left: Bode-plot at 30°C of the cold-densified powder. At low frequency pure ohmic conduction is present. Right: time dependent decrease of electron conduction due to insufficient bracing of the cell. Line to guide the eye.

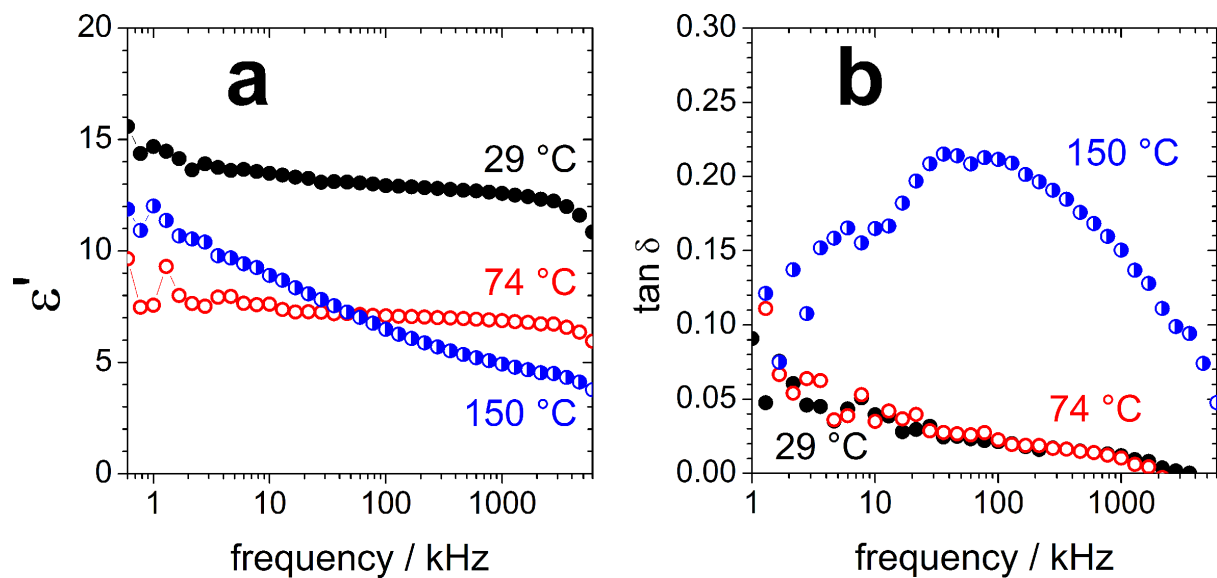


Figure S11. Frequency dependence of the real part (ϵ') of complex permittivity (a) and the dielectric loss $\tan \delta$ (b) at different temperatures.

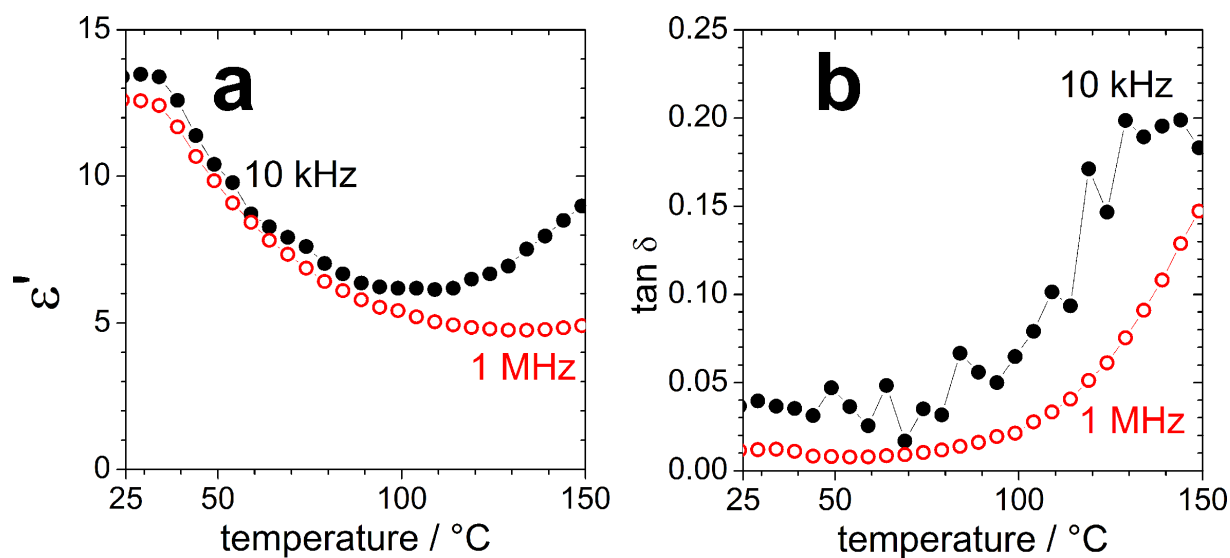


Figure S12. Temperature dependence of the real part (ϵ') of complex permittivity (a) and dielectric loss $\tan \delta$ (b) at selected frequencies.

NMR Spectroscopy

NMR spectroscopic measurements were conducted on washed $\text{LiLa}_2\text{NH}_2\text{O}$, $\text{LiLa}_2\text{ND}_2\text{O}$ and $\text{LiLa}_2\text{N}_{1.5}\text{D}_{2.5}$ specimens and compared with the related deuteride oxides LiLa_2DO_3 and $\text{LiSrLaD}_2\text{O}_2$ to investigate the short-range ordering of hydrogen and deuterium atoms in the crystal structure. In $\text{LiLa}_2\text{NH}_2\text{O}$, the calculated static ^1H linewidth full width at half maximum based on dipolar coupling only via the second moment is much larger than the experimental linewidth (73 kHz compared to 37 kHz; Figure S13). For $\text{LiLa}_2\text{ND}_2\text{O}$, $\text{LiLa}_2\text{N}_{1.5}\text{D}_{2.5}$, LiLa_2DO_3 , and $\text{LiSrLaD}_2\text{O}_2$, the calculated static ^2H linewidths show the inverse effect: the calculated values are smaller than the experimental ones (Table S4). Additionally, the static ^2H spectra of $\text{LiLa}_2\text{N}_{1.5}\text{D}_{2.5}$ show two distinct signals which either result from the two distinct crystallographic deuterium sites or two types of deuterium atoms with different mobility. For ^2H , quadrupolar coupling is an additional factor in contrast to ^1H , though the calculated quadrupolar coupling constants of ^2H based on the local surroundings of lithium and lanthanum atoms are larger than the experimental ones (Figure S14, Table S3). For $\text{LiLa}_2\text{N}_{1.5}\text{D}_{2.5}$, only one signal is found in the MAS spectrum irrespective of the two deuterium sites in the crystal structure. Given the residual linewidth in MAS experiments and the small shift range for ^2H , the two lines seem to be superimposed.

The ^7Li spectra of both $\text{LiLa}_2\text{ND}_2\text{O}$ and $\text{LiLa}_2\text{N}_{1.5}\text{D}_{2.5}$ are dominated by quadrupolar coupling (Figures S15, top left and right). The contribution of dipolar coupling to the linewidth is combined from all active nuclei at less than 9 kHz. Like the ^2H case, the calculated ^7Li quadrupolar coupling constants for the different scenarios exceed the experimental linewidths. For $\text{LiLa}_2\text{ND}_2\text{O}$, the MAS lineshape can be fitted to a quadrupolar coupling of $C_Q = 100$ kHz and $\eta = 1$. However, the static lineshape (data not shown) indicates a superposition of different linewidths or the resulting linewidth due to a dynamic process. For the calculation of the quadrupole coupling, different scenarios are calculated based on the occupancy factors for O/N and D. Resulting values range between 70 kHz (Li surrounded by 4 D and 2 O atoms) and 470 kHz (Li surrounded by 3 D and 2 N atoms). On average, considering the relative probability of the different scenarios, a coupling of 130 kHz would result.

In the case of $\text{LiLa}_2\text{N}_{1.5}\text{D}_{2.5}$, similar observations are made. The MAS lineshape shows good agreement with an assumed quadrupolar coupling constant of 30 kHz. Calculated quadrupolar couplings are averaged 240 kHz with scenarios ranging from 500 kHz (6 D atoms surrounding) to 20 kHz (4 D and 2 N atoms). The hydride oxides LiLa_2DO_3 and $\text{LiSrLaD}_2\text{O}_2$ show comparable discrepancies between experimental and calculated signal width (Table S4; Figure S15, bottom). For all nuclei, the discrepancies between calculated and experimental linewidth are similar for non-washed samples, i.e. it does not result from a partial hydrolysis of the samples.

As quadrupolar coupling is usually insignificant for ionic hydrides,^[38] there might be a significant covalent contribution to the bonding of deuterium and lithium atoms. The discrepancies between the experimental and calculated static linewidths and quadrupolar coupling constants might furthermore stem from mobile hydrogen and deuterium atoms, as expected from the crystal structure. Since the linewidth of $\text{LiLa}_2\text{ND}_2\text{O}$, LiLa_2DO_3 and $\text{LiSrLaD}_2\text{O}_2$ remained constant upon

cooling to 210 K and significant hydride conduction in LiLa_2HO_3 and $\text{LiSrLaH}_2\text{O}_2$ is only reported for much higher temperatures ($> 473 \text{ K}$)^[16,37] these discrepancies might also hint at an incomplete description of the quadrupolar coupling by the employed point charge assumption for the calculation of the electric field gradient. A more complex approach might be required here, which is however beyond the scope of this work.

Table S4. Experimental (exp.) and calculated (calc.) static dipolar and MAS quadrupolar coupling constants of $\text{LiLa}_2\text{ND}_2\text{O}$, $\text{LiLa}_2\text{N}_{1.5}\text{D}_{2.5}$, LiLa_2DO_3 , and $\text{LiSrLaD}_2\text{O}_2$ based on solid state NMR measurements at room temperature.

Compound	^2H static linewidth ^[a] / kHz		^2H quadrupolar coupling constant $C_Q^{[b]}$ / kHz		^7Li quadrupolar coupling constant $C_Q^{[b]}$ / kHz	
	exp.	calc.	exp.	calc.	exp.	calc.
$\text{LiLa}_2\text{ND}_2\text{O}$	13.0	6.2	14	27	100	70–470
$\text{LiLa}_2\text{N}_{1.5}\text{D}_{2.5}$	2.5, 12.9	3.8 (D1), 6.2 (D2)	10	16 (D1), 26 (D2)	30	20–500
LiLa_2DO_3	11.9	6.1	12	22	140	470
$\text{LiSrLaD}_2\text{O}_2$	17.2	6.3	13	16–26	10	26–71

[a]: based on static measurements. Calculations based on the second moment considering only dipolar coupling.

[b]: based on MAS measurements.

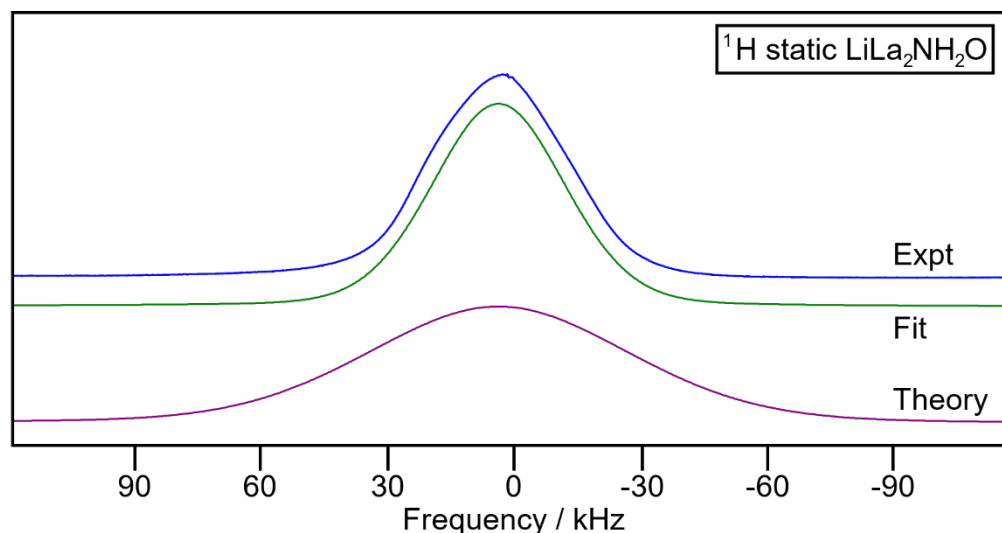


Figure S13. Static ^1H NMR spectrum of washed $\text{LiLa}_2\text{NH}_2\text{O}$ in addition to fit and simulation based on dipole coupling.

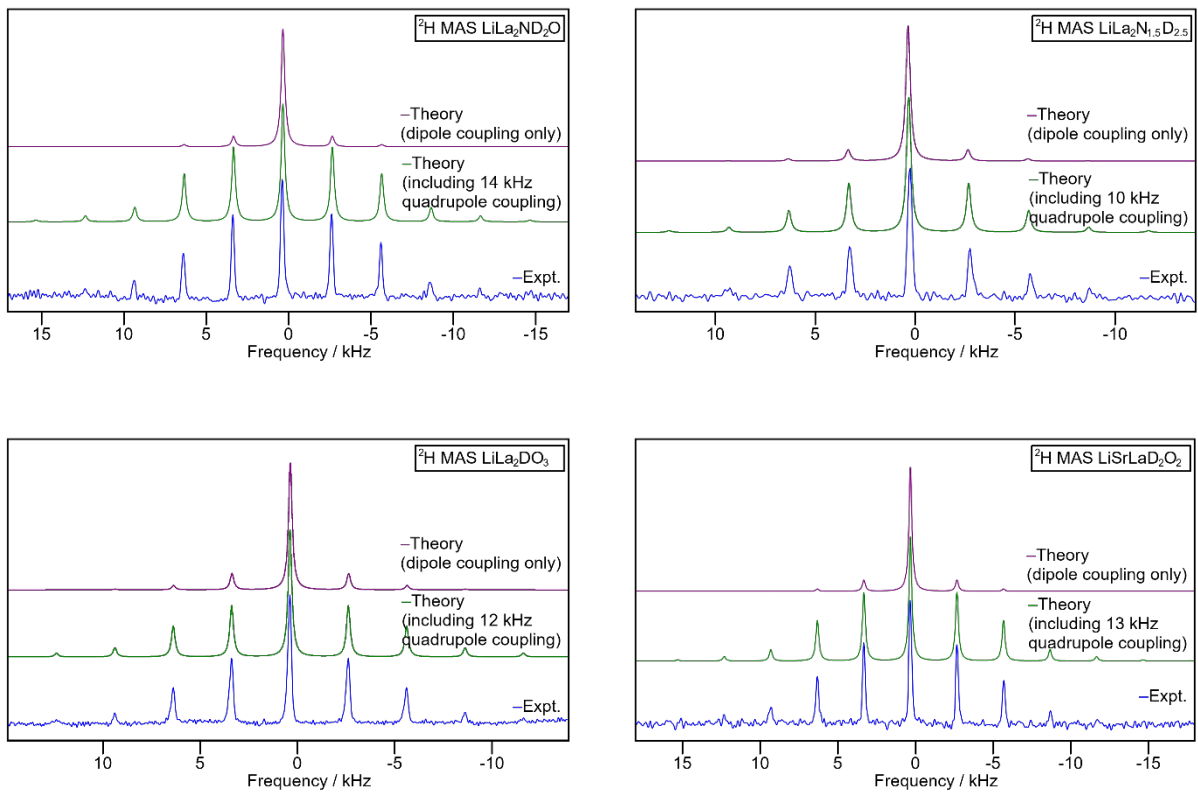


Figure S14. ^2H NMR-MAS spectra of washed $\text{LiLa}_2\text{ND}_2\text{O}$ (top left), $\text{LiLa}_2\text{N}_{1.5}\text{D}_{2.5}$ (top right), LiLa_2DO_3 (bottom left), and $\text{LiSrLaD}_2\text{O}_2$ (bottom right) specimen in addition to simulations based on dipole- and quadrupole coupling.

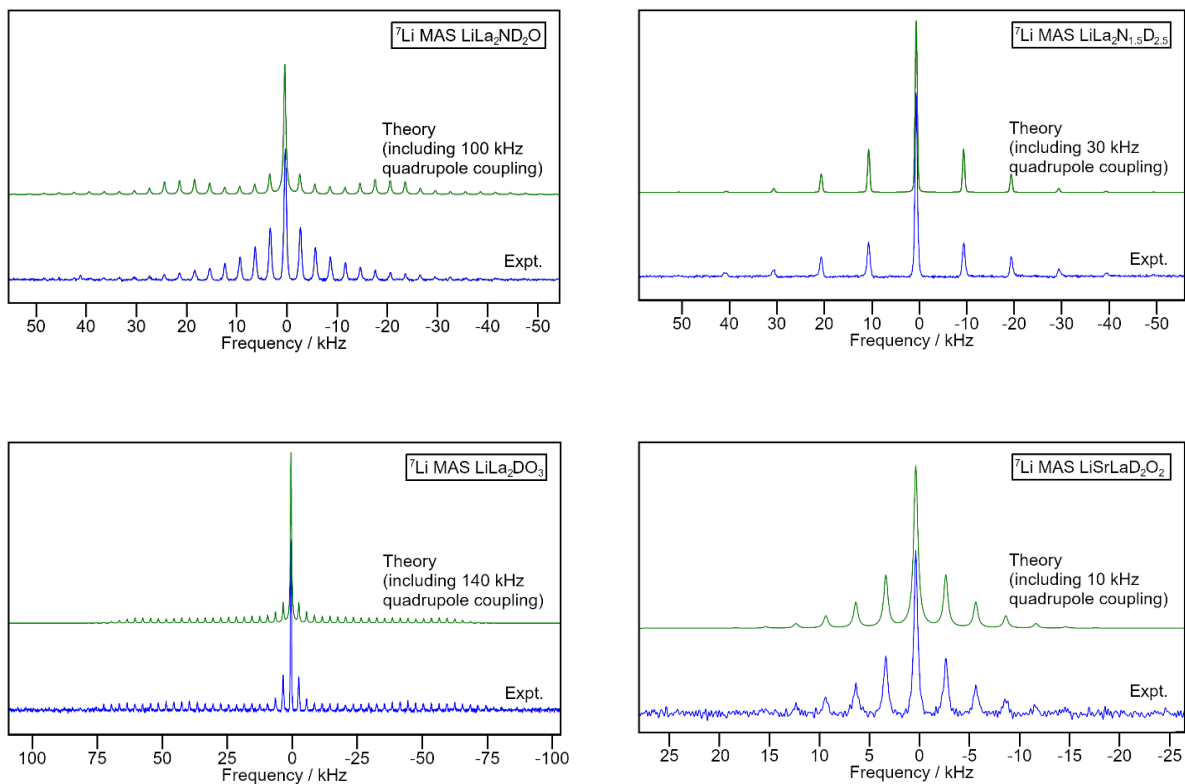


Figure S15. ${}^7\text{Li}$ NMR-MAS spectra of washed $\text{LiLa}_2\text{ND}_2\text{O}$ (top left), $\text{LiLa}_2\text{N}_{1.5}\text{D}_{2.5}$ (top right), LiLa_2DO_3 (bottom left), and $\text{LiSrLaD}_2\text{O}_2$ (bottom right) specimen in addition to simulations based on dipole- and quadrupole coupling. Mind the different x-scalings of the individual graphs.

References

- [1] H. Kohlmann, C. Hein, R. Kautenburger, T. C. Hansen, C. Ritter, S. Doyle, *Z. Kristallogr.* **2016**, *231*, 517-523.
- [2] B. Song, J. K. Jian, G. Wang, M. Lei, Y. P. Xu, X. L. Chen, *Chem. Mater.* **2007**, *19*, 1497-1502.
- [3] G. Brauer in *Handbuch der Präparativen Anorganischen Chemie, Vol. II* (Eds.: G. Brauer), Ferdinand Enke Verlag, Stuttgart, **1975**, pp. 29-33.
- [4] N. Matsui, G. Kobayashi, K. Suzuki, A. Watanabe, A. Kubota, Y. Iwasaki, M. Yonemura, M. Hirayama, R. Kanno, *J. Am. Chem. Soc.* **2018**, *102*, 3228-3235.
- [5] N. Matsui, Y. Hinuma, Y. Iwasaki, K. Suzuki, J. Guangzhong, H. Nawaz, Y. Imai, M. Yonemura, M. Hirayama, G. Kobayashi, *J. Mater. Chem. A* **2020**, *8*, 24685-24694.
- [6] a) H. M. Rietveld, *Acta Crystallogr.* **1967**, *22*, 151-152; b) H. M. Rietveld, *J. Appl. Crystallogr.* **1969**, *2*, 65-71.
- [7] J. Rodríguez-Carvajal, *Physica B* **1993**, *192*, 55-69.
- [8] a) G. Kresse, J. Furthmüller, *Comput Mater. Sci.* **1996**, *6*, 15-50; b) G. Kresse, J. Furthmüller, *Phys. Rev. B: Condens. Matter Mater. Phys.* **1996**, *54*, 11169-11186.
- [9] P. E. Blöchl, *Phys. Rev. B: Condens. Matter Mater. Phys.* **1994**, *50*, 17953-17979.
- [10] J. P. Perdew, K. Burke, M. Ernzerhof, *Phys. Rev. Lett.* **1996**, *77*, 3865-3868.
- [11] P. E. Blöchl, O. Jepsen, O. K. Andersen, *Phys. Rev. B: Condens. Matter Mater. Phys.* **1994**, *49*, 16223-16233.
- [12] D. Massiot, F. Fayon, M. Capron, I. King, S. Le Calv'e, B. Alonso, J.-O. Durand, B. Bujoli, Z. Gan, G. Hoatson, *Magn. Reson. Chem.* **2002**, *40*, 70-76.
- [13] J. H. van Vleck, *Phys. Rev.* **1948**, *74*, 1168.
- [14] R. D. Stoddard, M. S. Conradi, *Phys. Rev. B* **1998**, *57*, 10455-10461.
- [15] S. H. Choh, H. W. Shin, I.-W. Park, H. Ju, J. H. Kim, J. H. Kim, *J. Korean Magn. Reson. Soc.* **2003**, *7*, 16-24.
- [16] G. Kobayashi, Y. Hinuma, S. Matsuoka, A. Watanabe, M. Iqbal, M. Hirayama, M. Yonemura, T. Kamiyama, I. Tanaka, R. Kanno, *Science* **2016**, *351*, 1314-1317.
- [17] D. Liu, Q. Liu, T. Si, Q. Zhang, *J. Alloys Compd.* **2010**, *495*, 272-274.
- [18] B. Malaman, J. Brice, *J. Solid State Chem.* **1984**, *53*, 44-54.
- [19] J. Songster, A. D. Pélton, *J. Phase Equilibria* **1993**, *14*, 373-381.

- [20] H. Schwarz, Neuartige Hydrid-Oxide der Seltenen Erden: Ln_2LiHO_3 mit $\text{Ln} = \text{La}, \text{Ce}, \text{Nd}, \text{Pr}$ und Nd , doctoral dissertation, Karlsruhe University, **1991**.
- [21] F. Gehlhaar, R. Finger, N. Zapp, M. Bertmer, H. Kohlmann, *Inorg. Chem.* **2018**, *57*, 11851-11854.
- [22] Ø. S. Fjellvåg, K. H. Nygård, P. Vajeeston, A. O. Sjøstad, *Chem. Commun.* **2019**, *55*, 3817-3820.
- [23] N. Zapp, Rare Earth Heteroanionic Hydrides with Secondary O^{2-} , F^- , and N^{3-} -Ions Related to the CaF_2 - and K_2NiF_4 -Structure Types, doctoral dissertation, Leipzig University, **2021**.
- [24] V. F. Sears, *Neutron News* **1992**, *3*, 26-37.
- [25] R. Niewa, D. Zherebtsov, *Z. Kristallogr.* **2002**, *217*, 317-318.
- [26] a) J. P. Vidal, G. Vidal-Valat, *Acta Crystallogr. B* **1986**, *42*, 131-137; b) Z. Li, J. Zhang, M. Latroche, S. Wang, L. Jiang, J. Du, F. Cuevas, *Phys. Chem. Chem. Phys.* **2016**, *18*, 23944-23953; c) R. S. Calder, W. Cochran, D. Griffiths, R. D. Lowde, *J. Phys. Chem. Solids* **1962**, *23*, 621-632.
- [27] A. Huq, J. W. Richardson, E. R. Maxey, D. Chandra, W.-M. Chien, *J. Alloys Compd.* **2007**, *436*, 256-260.
- [28] T. Farley, W. Hayes, S. Hull, M. Hutchings, M. Vrtis, *J. Phys. Condens. Matter* **1991**, *3*, 4761.
- [29] B. Blaschkowski, T. Schleid, *Z. anorg. allg. Chem.* **2007**, *633*, 2644-2648.
- [30] T. Udovic, Q. Huang, J. Rush, *J. Solid State Chem.* **1996**, *122*, 151-159.
- [31] K. Conder, W. Longmei, E. Borocho, E. Kaldis, J. Schefer, *Eur. J. Solid State Inorg. Chem.* **1991**, *28*, 487-494.
- [32] G. Schiller, Die Kristallstrukturen von Ce_2O_3 (A-Form), LiCeO_2 und CeF_3 - Ein Beitrag zur Kristallchemie des dreiwertigen Cers, doctoral dissertation, Karlsruhe university, **1985**.
- [33] F. Gehlhaar, R. Finger, N. Zapp, M. Bertmer, H. Kohlmann, *Inorg. Chem.* **2018**, *57*, 11851-11854.
- [34] a) V. P. Ting, P. F. Henry, H. Kohlmann, C. C. Wilson, M. T. Weller, *Phys. Chem. Chem. Phys.* **2010**, *12*, 2083-2088; b) J. D. Dunitz, R. M. Ibberson, *Angew. Chem. Int. Ed.* **2008**, *47*, 4208-4210.
- [35] J. T. S. Irvine, D. C. Sinclair, A. R. West, *Adv. Mater.* **1990**, *2*, 132-138.
- [36] a) K. Wu, W. A. Schulze, *J. Am. Ceram. Soc.* **1992**, *75*, 3390-3395; b) F. Oehler, H.-T. Langhammer, S. G. Ebbinghaus, *J. Eur. Ceram. Soc.* **2017**, *37*, 2129 – 2136.
- [37] a) Y. Iwasaki, N. Matsui, K. Suzuki, Y. Hinuma, M. Yonemura, G. Kobayashi, M. Hirayama, I. Tanaka, R. Kanno, *J. Mater. Chem. A* **2018**, *6*, 23457-23463; b) N. Matsui, Y. Hinuma, Y.

Iwasaki, K. Suzuki, J. Guangzhong, H. Nawaz, Y. Imai, M. Yonemura, M. Hirayama, G. Kobayashi, R. Kanno, *J. Mater. Chem. A* **2020**, *8*, 24685-24694;

- [38] a) A. J. E. Rowberg, C. G. Van de Walle, *ACS Appl. Energy Mater.* **2021**, *4*, 6348-6355; b) Ø. S. Fjellvåg, M. Krzystyniak, P. Vajeeston, A. O. Sjøstad, J. Armstrong, *J. Phys. Commun.* **2019**, *3*, 103002; c) F. Takeiri, A. Watanabe, A. Kuwabara, H. Nawaz, N. I. P. Ayu, M. Yonemura, R. Kanno, G. Kobayashi, *Inorg. Chem.* **2019**, *58*, 4431-4436; d) H. Nawaz, F. Takeiri, A. Kuwabara, M. Yonemura, G. Kobayashi, *Chem. Commun.* **2020**, *56*, 10373-10376; e) H. W. T. Morgan, H. J. Stroud, N. L. Allan, *Chem. Mater.* **2021**, *33*, 177-185.
- [38] a) H. Auer, R. Guehne, M. Bertmer, S. Weber, P. Wenderoth, T. C. Hansen, J. Haase, H. Kohlmann, *Inorg. Chem.* **2017**, *56*, 1061-1071; b) R. Guehne, H. Auer, H. Kohlmann, J. Haase, M. Bertmer, *Phys. Chem. Chem. Phys.* **2019**, *21*, 10594-10602.

Author Contributions

N. Zapp	Concept, synthesis, collection of XRPD data, diffraction data analysis and interpretation, DFT calculations, writing of original draft; lead contribution
F. Oehler	Collection, procession, analysis and discussion of temperature dependent impedance spectra; supporting contribution
M. Bertmer	Collection, procession, analysis and discussion of NMR data; supporting contribution
H. Auer	Collection, procession, analysis and discussion of room temperature impedance spectra, supporting contribution
D. Sheptyakov	Collection and procession of neutron diffraction data; supporting contribution
C. Ritter	Collection and procession of neutron diffraction data; supporting contribution
H. Kohlmann	Supervision, data interpretation, funding acquisition, project administration; supporting contribution